Circulation-driven variability of Atlantic anthropogenic carbon transports and uptake

Peter J. Brown[1*], Elaine L. McDonagh[1,2], Richard Sanders[1,2], Andrew J. Watson[3], Rik Wanninkhof[4], Brian A. King[1], David A. Smeed[1], Molly O. Baringer[4], Christopher S. Meinen[4], Ute Schuster[3], Andrew Yool[1], Marie-José Messias[3].

1. National Oceanography Centre, Southampton, UK
2. NORCE, Norwegian Research Centre, Bjerknes Centre for Climate Research, Bergen, Norway
3. College of Life and Environmental Sciences, University of Exeter, Exeter, UK
4. NOAA / Atlantic Oceanographic and Meteorological Laboratory, Miami, Florida, USA

The ocean absorbs approximately a quarter of the carbon dioxide currently released to the atmosphere by human activities (C_{anth}). A disproportionately large fraction accumulates in the North Atlantic due to the combined effects of transport by the Atlantic Meridional Overturning Circulation (AMOC) and air-sea exchange. However, discrepancies exist between modelled and observed estimates of the air-sea exchange due to unresolved ocean transport variability. Here we quantify the strength and variability of C_{anth} transports across 26.5°N in the North Atlantic between 2004 and 2012 using circulation measurements from the RAPID mooring array and hydrographic observations. Over this time period, decreasing circulation strength tended to decrease northward C_{anth} transport, while increasing C_{anth} concentrations (preferentially in the upper limb of the overturning circulation) tended to increase northward C_{anth} transport. These two processes

compensated each other over the 8.5-year period. While ocean transport and air-sea C_{anth} fluxes are approximately equal in magnitude, the increasing accumulation rate of C_{anth} in the North Atlantic combined with a stable ocean transport supply means we infer a growing contribution from air-sea C_{anth} fluxes over the time period. North Atlantic C_{anth} accumulation is thus sensitive to AMOC strength, but growing atmospheric C_{anth} uptake continues to significantly impact C_{anth} transports.

The ocean exchanges carbon dioxide (CO_2) rapidly with the atmosphere, with regions of substantial net CO_2 uptake and release created by ocean circulation, biological processes and heat and freshwater fluxes[1]. In pre-industrial times the global net CO_2 flux from the ocean to the atmosphere is estimated to have been ~0.45-0.78 Pg C yr^{-1} balancing riverine carbon inputs[2,3]. However, increasing atmospheric CO_2 concentrations since the beginning of the Industrial Revolution have reversed the flux, transferring anthropogenic carbon (C_{anth}) into the ocean at a rate of 2.6 ± 0.3 Pg C yr^{-1} [4], slowing the accumulation of anthropogenic CO_2 in the atmosphere and reducing the pace of global warming. This net global oceanic C_{anth} uptake accounts for nearly 50% of all historical fossil fuel emissions[5] and 23% of total contemporary emissions[6]. Understanding the processes that cause this uptake to occur and their susceptibility to change are therefore high priority activities.

The North Atlantic (NA) and Arctic region (from the equator to Bering Strait) is a key region as it plays a disproportionately large role in the uptake of both CO_2 and C_{anth} from the atmosphere. It was a regional sink for atmospheric carbon in pre-industrial times[7], and now accounts for approximately 25% of all contemporary global CO_2 uptake from the atmosphere[6,8] and 25% of the global ocean C_{anth} inventory[4,5,9,10] despite having only 15% of the global ocean surface. The "natural" (i.e. pre-industrial) CO_2 uptake results from both the surface cooling of warm water advected polewards prior to sinking, as part of the Atlantic Meridional Overturning Circulation (AMOC, see Figure 1, adapted from [11]), and from strong biological production[12]. The AMOC generates a net southwards transport of contemporary (natural and anthropogenic) carbon, with lower carbon concentrations in the warm, upper northward flow being exceeded by higher concentrations in the cold, deep return flow[7,13]. Conversely, the post-industrial build-up of C_{anth} in surface waters generates a surface-enhanced concentration profile (Figure 1 for C_{anth} distribution along 26.5°N); when combined with the action of the overturning circulation this leads to a net northwards transport of C_{anth} into the NA[13,14], the opposite direction to the natural carbon transport and contributes to the highest regional C_{anth} accumulation rates in the global ocean[4,5].

The size, variability and controls of the ocean circulation contribution to regional C_{anth} storage and hence the resilience of this sink to global change are largely unknown. Prior observational estimates of NA C_{anth} accumulation, from individual synoptic repeat hydrographic sections, vary widely (0.19-0.43 Pg C yr^{-1} [13–17], Table 1), with more constrained estimates only possible through larger-scale, regional/global analyses (0.38-0.47 Pg C yr^{-1}, based on analyses of ocean inversion and data assimilation models or observational integrations[4,10,18]). Cruise-based estimates of northwards ocean C_{anth} transports meanwhile (0.17-0.25 Pg C yr^{-1} [13–17]) are typically much higher than estimates from biogeochemical models, ocean inversions and data assimilations (0.09-0.15 Pg C yr^{-1} [4,10,18–20]); this is primarily due to cruise-based C_{anth} transport estimates being based on single "snapshot" estimates of ocean circulation (principally the AMOC), and the inability of biogeochemical models and data assimilations to correctly estimate volume transports[19]. Between 27% and 66% of C_{anth} accumulation is thus driven by the northward ocean transport (the remainder being taken up from the atmosphere). The magnitude of the range is indicative of the uncertainty related to unresolved temporal variability, observational and methodological limitations, and that each estimate is associated with a single state of the circulation or AMOC strength.

It is now clear that individual snapshot estimates of AMOC strength used in previous calculations of C_{anth} uptake (variability of which is removed by the inversion/ assimilation techniques described above) do not fully capture true circulation variability[21]. The AMOC estimated from the RAPID-MOCHA-WBTS programme at 26.5°N[21] (Figure 1) had an average strength of 17.2 Sv over the 2004-2012 period, with substantial temporal variability (10 day filtered root mean square variability of 4.6 Sv, variability of annual means of 2.2 Sv)[21,22]. However this variability was superimposed on a significant decreasing trend in AMOC magnitude of -0.54 Sv yr^{-1} which occurred over the same time period[23,24]. CMIP5 Earth System models have predicted that weakening of AMOC strength similar in scale to this recently observed will lead to a decline in both surface CO_2 uptake and accumulation at depth as climate change feedbacks strengthen[25].

High frequency anthropogenic carbon transport estimates

Here we investigate the impact of observed circulation change on C_{anth} accumulation in the NA between 2004 and 2012 , combining 10-day AMOC transport fields at 26.5°N[21,26] with C_{anth} concentrations estimates. A time-series of C_{anth} concentration distributions is generated using regressions constructed from all available hydrographic data at 26.5°N and applied to the RAPID-Argo 10-day temperature-salinity fields[26] (see Methods, Extended Data Figures 1-3, Extended Data Table 1). Therefore, it includes variability associated with the changing distribution of water masses on the section (from RAPID and Argo) and longer-term, water mass-specific concentration trends (from repeat hydrography). In addition, in the upper 200m of the water column we incorporate a new Scaled PreIndustrial DisEquilibrium (SPIDEr) method based on sea-surface pCO_2 observations to account for seasonal variation of the C_{anth} concentration that has not been included in previous treatments[15]; this ensures feasible year-round concentration ranges that are consistent with Revelle factor (R*f*) variability and air-sea fluxes (Methods, Extended Data Figures 4-5). For the region east of the Bahamas, estimated C_{anth} distributions are combined with 10-day mooring/float derived transport fields, while in Florida Straits we calculate a transport-weighted C_{anth} (C_{anth} transport divided by volume transport) time-series from repeat hydrographic sections that enables combination with the submarine cable-derived transport time-series (Methods, Extended Data Figure 6). Uncertainties in C_{anth} transports were calculated following the approach used for freshwater transport[26] but also accounting for uncertainties associated with C_{anth} estimation and trends (Methods, Extended Data Table 2). The uncertainty in volume transport contributes 70% to the total error estimate, with uncertainties relating to the C_{anth} concentrations contributing approximately 30%. We analysed the robustness and appropriateness of the methodology employed for estimating C_{anth} and its transport for the time between hydrographic sections by using model outputs. Predicted C_{anth} transport fields (generated as for observations, using predictive parameterisations of model 'truth' C_{anth}) were compared with explicitly determined model C_{anth} transport fields (based on parallel NEMO-MEDUSA 1° model runs with and without atmospheric CO_2 growth and with identical physical fields), and suggested the approach can reproduce the 2004-2012 model mean to within 3% of the model truth, and shorter-term estimates (1 month) to within ~9% (worst-case) (Methods, Extended Data Figure 7). Finally, we tested the back-calculation C_{anth} estimation method employed on hydrographic data by direct application to model outputs; results showed accuracy to within 0.5% for the 2004-2012 C_{anth} transport model mean and to within ~7% for shorter, 1-month estimates (Methods, Extended Data Figure 8).

Circulation components of anthropogenic carbon transport

Figure 2 summarizes the transport of C_{anth} across the 26.5°N section. A mean northwards C_{anth} transport is calculated for 2004-2012 of 0.191 ± 0.013 Pg C yr^{-1} (mean ± total uncertainty in time-series mean, Figure 2a black line, Extended Data Table 2, Methods). This lies within the range of previous estimates determined from hydrography, but is larger than that derived from inversion models (Table 1). The mean net C_{anth} transport is largely set by the difference between the northward Florida Straits transport and the southward interior transport between 0-1100 db, the two largest transport components (Figure 2a, Table 2). Although the mean volume transport in Florida Straits (31.6 Sv) is greater than the geostrophic interior transport (-18.6 Sv) the transport-weighted C_{anth} for the interior (65.6 μmol kg^{-1}) is higher than that for Florida Straits (54.4 μmol kg^{-1}), reflective of the accumulation of C_{anth} in surface waters as they recirculate in the anticyclonic gyre from the western boundary (Figure 1). Contributions from northwards Ekman C_{anth} transports (3.5 Sv, driven by surface winds and calculated from ERA-Interim data) enhance the net total C_{anth} transport, and show strong variability and occasional southward incursions. While the combined transports between 1100-5000 db (-18.7 Sv) make up the smallest contribution to the overall C_{anth} transport (southward export of 0.09 Pg C yr^{-1}, transport-weighted C_{anth} 12.5 μmol kg^{-1}, Table 2, Figure 2a), they do represent the NA's input to long-term storage of carbon in the deep ocean, equivalent to 4% of the total annual global C_{anth} uptake rate[4]. There is a high degree of variability over the 8.5-year record, with a maximum annual peak-to-peak amplitude of 0.48 Pg C yr^{-1} (Dec 2008 to Dec 2009, Figure 2a/d), a standard deviation of 10-day transport estimates of 0.08 Pg C yr^{-1} and substantial interannual variability with annual means ranging from 0.11 to 0.23 Pg C yr^{-1} (Figure 2b). Application of a 3-month low-pass filter reveals a strong seasonal cycle (amplitude 0.08 Pg C yr^{-1}, Figure 2c).

Following methods used for freshwater[26] we additionally separated C_{anth} transport into overturning, horizontal and throughflow components (Figure 2d) as an indication of the dominant components of C_{anth} transport strength and variability: overturning describes the transport's vertical structure (zonally-averaged C_{anth} and velocity fields with the section average removed), horizontal represents the gyre and eddy transports (calculated as the total C_{anth} transport with mean and overturning contributions removed), and throughflow represents the ~0.8 Sv of Pacific water that flows southwards through the Atlantic from Bering Strait (see Methods for details). The throughflow component is almost zero for C_{anth} (-0.8 Tg C yr^{-1}, 1000 Tg=1Pg) as per previous studies[13,15] and is not shown. The overturning C_{anth} transport is northwards (mean ± standard deviation: +0.31 ± 0.09 Pg C yr^{-1}), its sign representative of the upper ocean northward limb having higher C_{anth} concentrations than its deep, southward-flowing limb (Figure 1, Table 2).

The horizontal C_{anth} transport is southwards (mean ± standard deviation: -0.11 ± 0.02 Pg C yr^{-1}) and derives from the west-east C_{anth} concentration gradient combining with both the north- and southward gyre and eddy transports, and the horizontal component of the Florida Straits transport being compensated by southward flow in the upper ocean of the interior east of the Bahamas. The horizontal C_{anth} transport component is smaller in magnitude and less variable than the overturning component (Figure 2d), with AMOC volume transport variability describing 80% of the variance in C_{anth} transports. This strong AMOC:C_{anth} transport correlation at 26.5°N (Figure 3a) is supported by model outputs[19] and here indicates a 1 Sv increase in overturning is associated with an 18 Tg C yr^{-1} increase in C_{anth} transport. There is temporal structure in the correlation's residual (Figure 3b) with the residual growing over the length of the time-series; this represents that part of the variability that is not correlated with the AMOC (such as increasing C_{anth} loadings) and can be interpreted as an increase in the sensitivity of C_{anth} transports per Sverdrup of AMOC.

Despite increasing C_{anth} concentrations there is no trend in the total C_{anth} transport across 26.5°N between 2004-2012. Significant trends are however present in the subregions, with the largest (and near-compensating) trends associated with the two largest components (positive trend, Florida Straits; negative trend, upper mid-ocean, Table 2). Although the C_{anth} transport-AMOC correlation and a decrease in AMOC strength of -0.54 Sv yr^{-1} observed between 2004-2012[23] predicts a decreasing overturning component trend (-10 Tg C yr^{-2}), the observed value is much smaller (-6 Tg C yr^{-2}) due to increasing C_{anth} concentrations. The overturning trend is not replicated in the total C_{anth} transport trend (-0.4 Tg C yr^{-2}) due to a compensating trend in the horizontal gyre component (+5 Tg C yr^{-2}).

Circulation change and water column C_{anth} accumulation

We can separate the impact of circulation change and water column C_{anth} accumulation on total and component C_{anth} transports by removing water mass-specific C_{anth} trends from the predicted C_{anth} fields and recombining the residual with the volume transport estimates. The time-series generated represents the effect of volume transport trends on an unchanging C_{anth} field while the difference from the full transport time-series reflects the effect of additional C_{anth} load (Figure 4 and Table 2). For the total northwards C_{anth} transport, this shows that circulation changes cause a decline of -94 Tg C yr^{-1} over 8.5 years.

However, this is balanced by an increasing transport due to growing C_{anth} concentrations derived from air-sea exchange of 89 Tg C yr^{-1}. Together they generate a total C_{anth} transport with no significant trend, thus implying that for 2004-2012 C_{anth} increases are counter-balanced by the effect of circulation change on the total oceanic supply of C_{anth} to the NA. For individual C_{anth} transport components and subregions, Florida Straits and the upper ocean interior still dominate; the increasing northward trend in Florida Straits is driven by growing C_{anth} loads (19 Tg C yr^{-1}); the increasingly southward (negative) interior trend is ~⅓ due to increasing C_{anth} concentrations (-6 Tg C yr^{-1}) and ~⅔ due to volume transport decreases (-12 Tg C yr^{-1}).

The horizontal C_{anth} transport is increasing (becoming more northward) because the Florida Straits transport-weighted C_{anth} trend is larger than the trend in the interior. The difference in the trends is due to C_{anth} concentrations increasing faster at the western boundary than at the eastern boundary, thereby diminishing the west-to-east gradient (Figure 1). The decreasing trend in overturning volume transport over the period is produced by balancing increases in southward moving upper waters (-0.48 Sv yr^{-1}) and reductions in southward-moving deep waters (3000-5000 db; +0.48 Sv yr^{-1}). This then creates an associated reduction in the northward C_{anth} overturning transport.

North Atlantic anthropogenic carbon budget

For the NA and Arctic region (26.5°N to Bering Strait), a regional C_{anth} budget of ocean transport, storage and air-sea fluxes can be formed using a storage rate of 0.39-0.47 Pg C yr^{-1} for 2004[10,15,18]. Combining our derived northward transport across 26.5°N of 0.191 Pg C yr^{-1} with the total C_{anth} contribution through Bering Strait (0.008 Pg C yr^{-1})[15], suggests that lateral oceanic transport supplies between 42% and 51% of the C_{anth} accumulating in the NA and Arctic. The remainder of the storage term must then originate from air-sea uptake (0.19-0.27 Pg C yr^{-1}).

The dominant air-sea flux contribution calculated here compares well with estimates from ocean inversions[18] and ocean assimilations[10] for the same timeframe (0.28-0.35 Pg C yr^{-1}, Table 1), despite ocean C_{anth} transport estimates differing somewhat. However, it differs markedly from the only previous estimate from observations where ocean transport dominates and air-sea uptake supplies only 0.13 Pg C yr^{-1} (33%) to C_{anth} inventory growth for 2004[15]. This difference comes largely from our revised estimate of the ocean transport term that, as the time-series and our seasonal correction to the near-surface concentrations show, exhibits large seasonal and interannual variability which have not previously been taken into consideration and are aliased in hydrographic-only transport estimates.

Contemporary sea-to-air CO_2 flux estimates calculated using sea surface ΔpCO_2 observations suggest an annual uptake for the NA-Arctic region north of 14-18°N of -0.53-0.63 Pg C yr^{-1} for 2004[27,28] (regional extents differ somewhat from ours, due to the choice of latitudinal boundaries by previous studies). Our C_{anth} uptake estimate of -0.19-0.27 Pg C yr^{-1} constitutes 40% of this signal, with the remainder (mean ± range -0.35 ± 0.08 Pg C yr^{-1}) being the “natural” uptake that would also have existed pre-industrially, a value consistent with global inverse model outputs (natural air-sea CO_2 flux neglecting riverine contribution -0.33 ± 0.08 Pg C yr^{-1}, and C_{anth} air-sea flux -0.31 ± 0.08 Pg C yr^{-1} scaled to 2004)[18,29]. Our revised estimate for the C_{anth} transport into the region provides consistency between observational and model estimates of the anthropogenic and pre-industrial components of the NA’s uptake of atmospheric CO_2.

The results presented here establish a strong relationship between the strength of the Atlantic overturning circulation and the oceanic contribution to the growing NA C_{anth} inventory (as inferred from rising air-sea CO_2 uptake[28,30] and historical storage increases[31]), confirming the recent outputs of a biogeochemical model[19]. The northward C_{anth} transport is highly variable on both short (10 day) and annual time periods, but when averaged over a nearly-decadal period it shows no significant trend. Though as regional C_{anth} accumulation continues to increase[4], this implies a decrease in the relative contribution from northward ocean C_{anth} transport. This result places greater emphasis on air-sea fluxes as the means by which local C_{anth} storage rates are maintained.

The overturning circulation is still the primary conduit in the NA by which CO_2 is both absorbed from the atmosphere (the AMOC-related transport and fluxes of heat and nutrients drive the strength of both physical and biological carbon pumps) and C_{anth}-rich waters are isolated from the surface on extended timescales[12,32]. While the long-term NA carbon sink is currently thought to be tracking the atmospheric CO_2 increase[30], surface warming is beginning to affect the uptake capacity of the subtropics[33]. This change combined with predicted long-term changes in AMOC strength[34] and buffering capacity[35] imparts substantial uncertainty to the future behaviour of the North Atlantic carbon sink over the twenty-first century[20,25] and its ability to slow atmospheric CO_2 increase rates.

ONLINE CONTENT

Methods, along with any additional Extended Data display items and Source Data, are available in the online version of the paper; references unique to these sections appear only in the online paper

REFERENCES

1. Sarmiento, J. L. & Gruber, N. Carbon Cycle, CO□, and Climate. in *Ocean Biogeochemical Dynamics* 392–457 (Princeton Univ. Press Princeton, NJ, 2006).

2. Jacobson, A. R., Fletcher, S. E. M., Gruber, N., Sarmiento, J. L. & Gloor, M. A joint atmosphere-ocean inversion for surface fluxes of carbon dioxide: 1. Methods and global-

scale fluxes. *Global Biogeochem. Cycles* **21**, (2007).

3. Resplandy, L. *et al.* Revision of global carbon fluxes based on a reassessment of oceanic and riverine carbon transport. *Nat. Geosci.* **11**, 504–509 (2018).

4. Gruber, N. *et al.* The oceanic sink for anthropogenic CO 2 from 1994 to 2007. *Science (80-.).* **363**, 1193–1199 (2019).

5. Sabine, C. L. *et al.* The Oceanic Sink for Anthropogenic CO2. *Science (80-.).* **305**, 367 LP – 371 (2004).

6. Friedlingstein, P. *et al.* Global Carbon Budget 2019. *Earth Syst. Sci. Data* **11**, 1783–1838 (2019).

7. Broecker, W. S. & Peng, T. H. Interhemispheric transport of carbon dioxide by ocean circulation. *Nature* **356**, 587–589 (1992).

8. Landschützer, P., Gruber, N. & Bakker, D. C. E. *An observation-based global monthly gridded sea surface pCO2 and air-sea CO2 flux product from 1982 onward and its monthly climatology (NCEI Accession 0160558), Version 5.5*. (2020).

9. Khatiwala, S. *et al.* Global ocean storage of anthropogenic carbon. *Biogeosciences* **10**, 2169–2191 (2013).

10. Devries, T. The oceanic anthropogenic CO2 sink: Storage, air-sea fluxes, and transports over the industrial era. *Global Biogeochem. Cycles* **28**, 631–647 (2014).

11. Srokosz, M. a. & Bryden, H. L. Observing the Atlantic Meridional Overturning Circulation yields a decade of inevitable surprises. *Science (80-.).* **348**, 1255575–1255575 (2015).

12. Sarmiento, J., Gruber, N., Brzezinski, M. & Dunne, J. High-latitude controls of thermocline nutrients and low latitude biological productivity. *Nature* **427**, 56–60 (2004).

13. Macdonald, A. M., Baringer, M. O., Wanninkhof, R., Lee, K. & Wallace, D. W. R. A 1998–1992 comparison of inorganic carbon and its transport across 24.5°N in the Atlantic. *Deep Sea Res. Part II Top. Stud. Oceanogr.* **50**, 3041–3064 (2003).

14. Rosón, G., Ríos, A. F., Pérez, F. F., Lavın, A. M. & Bryden, H. L. Carbon distribution, fluxes, and budgets in the subtropical North Atlantic Ocean (24.5°N). *J. Geophys. Res.* **108**, 3144 (2003).

15. Pérez, F. F. *et al.* Atlantic Ocean CO2 uptake reduced by weakening of the meridional overturning circulation. *Nat. Geosci.* **6**, 146–152 (2013).

16. Álvarez, M., Ríos, A. F., Pérez, F. F., Bryden, H. L. & Rosón, G. Transports and budgets of total inorganic carbon in the subpolar and temperate North Atlantic. *Global Biogeochem. Cycles* **17**, 2-1-2–21 (2003).

17. Zunino, P. *et al.* Transports and budgets of anthropogenic CO 2 in the tropical North Atlantic in 1992-1993 and 2010-2011. *Global Biogeochem. Cycles* **29**, 1075–1091 (2015).

18. Mikaloff Fletcher, S. E. *et al.* Inverse estimates of anthropogenic CO 2 uptake, transport, and storage by the ocean. *Global Biogeochem. Cycles* **20**, n/a-n/a (2006).

19. Racapé, V. *et al.* Transport and storage of anthropogenic C in the North Atlantic Subpolar Ocean. *Biogeosciences* **15**, 4661–4682 (2018).

20. Tjiputra, J. F., Assmann, K. & Heinze, C. Anthropogenic carbon dynamics in the changing ocean. *Ocean Sci.* **6**, 605–614 (2010).

21. McCarthy, G. D. *et al.* Measuring the Atlantic Meridional Overturning Circulation at 26°N. *Prog. Oceanogr.* **130**, 91–111 (2015).

22. Cunningham, S. A. *et al.* Temporal variability of the Atlantic meridional overturning circulation at 26.5°N. *Science (80-.).* **317**, 935–938 (2007).

23. Smeed, D. A. *et al.* Observed decline of the Atlantic meridional overturning circulation 2004-2012. *Ocean Sci.* **10**, 29–38 (2014).

24. Smeed, D. A. *et al.* The North Atlantic Ocean Is in a State of Reduced Overturning. *Geophys. Res. Lett.* **45**, 1527–1533 (2018).

25. Schwinger, J. *et al.* Nonlinearity of Ocean Carbon Cycle Feedbacks in CMIP5 Earth System Models. *J. Clim.* **27**, 3869–3888 (2014).

26. McDonagh, E. L. *et al.* Continuous Estimate of Atlantic Oceanic Freshwater Flux at 26.5°N. *J. Clim.* **28**, 8888–8906 (2015).

27. Takahashi, T. *et al.* Climatological mean and decadal change in surface ocean pCO2, and net sea-air CO2 flux over the global oceans. *Deep Sea Res. Part II Top. Stud. Oceanogr.* **56**, 554–577 (2009).

28. Schuster, U. *et al.* An assessment of the Atlantic and Arctic sea–air CO_2 fluxes, 1990–2009. *Biogeosciences* **10**, 607–627 (2013).

29. Gruber, N. *et al.* Oceanic sources, sinks, and transport of atmospheric CO 2. *Glob. Biogeochem. Cycles* **23**, GB1005 (2009).

30. Mckinley, G. A., Fay, A. R., Takahashi, T. & Metzl, N. Convergence of atmospheric and North Atlantic carbon dioxide trends on multidecadal timescales. *Nat. Geosci.* **4**, 606–610 (2011).

31. Woosley, R. J., Millero, F. J. & Wanninkhof, R. Rapid anthropogenic changes in CO 2 and pH in the Atlantic Ocean: 2003-2014. *Global Biogeochem. Cycles* **30**, 70–90 (2016).

32. Steinfeldt, R., Rhein, M., Bullister, J. & Tanhua, T. Inventory changes in anthropogenic carbon from 1997–2003 in the Atlantic Ocean between 20°S and 65°N. *Global Biogeochem. Cycles* **23**, 1–11 (2009).

33. Fay, A. R. & McKinley, G. A. Global trends in surface oceanpCO2from in situ data. *Global Biogeochem. Cycles* **27**, 541–557 (2013).

34. Cheng, W., Chiang, J. C. H. & Zhang, D. Atlantic Meridional Overturning Circulation (AMOC) in CMIP5 Models: RCP and Historical Simulations. *J. Clim.* **26**, 7187–7197 (2013).

35. Halloran, P. R. *et al.* The mechanisms of North Atlantic CO2 uptake in a large Earth System Model ensemble. *Biogeosciences* **12**, 4497–4508 (2015).

36. Guallart, E. F., Pérez, F. F., Rosón, G. & Ríos, A. F. High spatial resolution Alkalinity and pH measurements along 24 . 5 ° N in 1992 Institut de Ciències del Mar , CSIC Passeig Marítim de la Barceloneta , 37-49 08003 Barcelona , Spain Instituto de Investigaciones Marinas , CSIC Eduardo Cabello , 6 Facultad . **5**, (2010).

37. Brown, P. J., Bakker, D. C. E., Schuster, U. & Watson, A. J. Anthropogenic carbon accumulation in the subtropical North Atlantic. *J. Geophys. Res.* **115**, C04016 (2010).

38. Schuster, U. *et al.* Measurements of total alkalinity and inorganic dissolved carbon in the Atlantic Ocean and adjacent Southern Ocean between 2008 and 2010. *Earth Syst. Sci. Data* **6**, 175–183 (2014).

39. Guallart, E. F. *et al.* Trends in anthropogenic CO2 in water masses of the Subtropical North Atlantic Ocean. *Prog. Oceanogr.* **131**, 21–32 (2015).

40. Wanninkhof, R. *et al.* Ocean acidification along the Gulf Coast and East Coast of the USA. *Cont. Shelf Res.* **98**, 54–71 (2015).

41. Olsen, A. *et al.* GLODAPv2.2019 – an update of GLODAPv2. *Earth Syst. Sci. Data* **11**, 1437–1461 (2019).

42. Vázquez-Rodríguez, M. *et al.* Anthropogenic carbon distributions in the Atlantic Ocean:

data-based estimates from the Arctic to the Antarctic. *Biogeosciences* **6**, 439–451 (2009).

43. Touratier, F., Azouzi, L. & Goyet, C. CFC-11, $\Delta^{14}C$ and ^3H tracers as a means to assess anthropogenic CO_2 concentrations in the ocean. *Tellus B* **59**, 318–325 (2007).

44. Gruber, N., Sarmiento, J. L. & Stocker, T. F. An improved method for detecting anthropogenic CO_2 in the oceans. *Global Biogeochem. Cycles* **10**, 809–837 (1996).

45. Waugh, D. W., Hall, T. M., Mcneil, B. I., Key, R. & Matear, R. J. Anthropogenic CO_2 in the oceans estimated using transit time distributions. *Tellus B Chem. Phys. Meteorol.* **58**, 376–389 (2006).

46. Yool, A., Oschlies, A., Nurser, A. & Gruber, N. A model-based assessment of the TrOCA approach for estimating anthropogenic carbon in the ocean. *Biogeosciences* **7**, 723–751 (2010).

47. de Boyer Montégut, C., Madec, G., Fischer, A., Lazar, A. & Iudicone, D. Mixed layer depth over the global ocean: An examination of profile data and a profile-based climatology. *J. Geophys. Res.* **109**, C12003 (2004).

48. Álvarez, M. & Gourcuff, C. Uncoupled transport of chlorofluorocarbons and anthropogenic carbon in the subpolar North Atlantic. *Deep Sea Res. Part I Oceanogr. Res. Pap.* **57**, 860–868 (2010).

49. Landschützer, P. *et al.* A neural network-based estimate of the seasonal to inter-annual variability of the Atlantic Ocean carbon sink. *Biogeosciences* **10**, 7793–7815 (2013).

50. Bakker, D. C. E. *et al.* A multi-decade record of high-quality fCO_2 data in version 3 of the Surface Ocean CO_2 Atlas (SOCAT). *Earth Syst. Sci. Data* **8**, 383–413 (2016).

51. GLOBALVIEW-CO_2. *Cooperative Atmospheric Data Integration Project - Carbon Dioxide; NOAA ESRL, Boulder, Colorado; [Also available on Internet via anonymous*

FTP to ftp.cmdl.noaa.gov, Path: ccg/co2/GLOBALVIEW]. (2011).

52. Körtzinger, A. Methods of Seawater Analysis, Chap. Determination of Carbon Dioxide Partial Pressure (pCO2). *Verlag Chemie* 149–158 (1999).

53. Kalnay, E. *et al.* The NCEP/NCAR 40-Year Reanalysis Project. *Bull. Am. Meteorol. Soc.* **77**, 437–471 (1996).

54. Takahashi, T. *et al.* Climatological distributions of pH, pCO2, total CO2, alkalinity, and CaCO3 saturation in the global surface ocean, and temporal changes at selected locations. *Mar. Chem.* **164**, 95–125 (2014).

55. van Heuven, S., Pierrot, D., Rae, J. W. B., Lewis, E. & Wallace, D. W. R. *MATLAB Program Developed for CO2 System Calculations, ORNL/CDIAC-105b*. (2011) doi:10.3334/CDIAC/otg.CO2SYS_MATLAB_v1.1.

56. Gruber, N. Anthropogenic CO2 in the Atlantic Ocean. *Global Biogeochem. Cycles* **12**, 165–191 (1998).

57. Martiny, A. C. *et al.* Strong latitudinal patterns in the elemental ratios of marine plankton and organic matter. *Nat. Geosci.* **6**, 279–283 (2013).

58. Baringer, M. O. N. & Larsen, J. C. Sixteen years of Florida Current transport at 27 N. *Geophys. Res. Lett.* **28**, 3179–3182 (2001).

59. Dee, D. P. *et al.* The ERA-Interim reanalysis: configuration and performance of the data assimilation system. *Q. J. R. Meteorol. Soc.* **137**, 553–597 (2011).

60. Couldrey, M. P., Oliver, K. I. C., Yool, A., Halloran, P. R. & Achterberg, E. P. On which timescales do gas transfer velocities control North Atlantic CO2 flux variability? *Global Biogeochem. Cycles* **30**, 787–802 (2016).

61. Álvarez, M., Ríos, A. F., Pérez, F. F., Bryden, H. L. & Rosón, G. Transports and budgets

of total inorganic carbon in the subpolar and temperate North Atlantic. *Global Biogeochem. Cycles* **17**, 1002 (2003).

62. Lee, K. *et al.* An updated anthropogenic CO2 inventory in the Atlantic Ocean. *Global Biogeochem. Cycles* **17**, art. no.-1116 (2003).

63. Brewer, P. G., Bradshaw, A. L., Shafer, D. K. & Williams, R. T. Measurements of total carbon dioxide and alkalinity in the North Atlantic Ocean in 1981. in *The Changing Carbon Cycle: A Global Analysis* (eds. Trabalka, J. R. & Reichle, D. E.) 348–370 (Springer, 1986).

CORRESPONDING AUTHOR

All correspondence and requests for materials should be addressed to P.J.B. (peter.brown@noc.ac.uk)

ACKNOWLEDGEMENTS

The authors are grateful for support from the UK Natural Environment Research Council through projects 'Radiatively Active Gases from the North Atlantic Region and Climate Change' (RAGNARoCC) NE/K00249X/1, 'Atlantic Biogeochemical Fluxes' (ABC-Fluxes) NE/M005046/1 and RAPID-AMOC ((P.J.B., E.L.M., B.A.K., R.S., A.J.W., U.S., M.-J.M, D.A.S.), the NOAA Global Ocean Monitoring and Observation Program (GOMO) (via the Western Boundary Time Series project; FundRef number 100007298) and the NOAA Atlantic Oceanographic and Meteorological Laboratory (M.O.B., C.S.M., R.W.).

AUTHOR CONTRIBUTIONS

E.L.M., B.A.K, R.S. and A.J.W designed the study. P.J.B performed the analysis. P.J.B., E.L.M., R.S. and A.J.W wrote the manuscript. D.S., U.S., M.O.B., C.S.M. and R.W. gave technical support and conceptual advice. M.O.B., C.S.M., A.Y., U.S. & M.-J.M. contributed observational data.

COMPETING INTERESTS

The authors declare no competing interests.

FGURE LEGENDS

Figure 1. Atlantic Meridional Overturning Circulation observing system mooring array at 26.5°N with 2010 anthropogenic carbon distribution. Ekman transport is represented by black arrows, warm water circulation in the top 1100m is represented by red arrows, and blue arrows represent the mainly southward flow of colder, deeper waters. Adapted from [11] – reprinted with permission from AAAS.

Figure 2. Anthropogenic carbon transports across 26.5°N in the subtropical North Atlantic. (a) Ten-day (normal) and three month low-pass (bold) time-series of C_{anth} transports in (from top to bottom): Florida Straits Gulf Stream (red), total transport (black), Ekman layer (blue), 3000-5000m (grey), 1100-3000m (yellow), and top 1100m (pink-magenta) from April 2004 to October 2012. (b) Annual averages and standard error of the mean of C_{anth} transports for April-March. (c) Seasonal cycle of C_{anth} transports using monthly data and 3 month low-pass filtered data, error envelope of 1 standard devation. (d) Ten-day (normal) and three month low-pass (bold) time-series of total anthropogenic carbon transport (black) and its overturning (blue) and horizontal (orange) components. Dashed lines indicate the linear trend over the same timeframe. Positive values indicate northwards transport.

Figure 3. AMOC-C_{anth} transport co-variability and non-AMOC variability. (a) Relationship between strength of meridional overturning circulation and magnitude of anthropogenic carbon transport at 26.5°N. Colour scale relates each data point to the time-series in Figure 1. Diamonds represent April to March annual means with AMOC values from ref 17. (b) Residual between

observed C_{anth} transport and that predicted by linear AMOC-C_{anth} transport relationship versus time, describing variability that does not vary coherently with the AMOC. Dotted line is the linear trend of this residual between April 2004 and October 2012.

Figure 4. Impact of increasing anthropogenic carbon concentrations on ocean C_{anth} transport. (a) Ten-day (normal) and three month low-pass (bold) time-series of total anthropogenic carbon transport including (red) and ignoring (blue) effect of C_{anth} accumulating in the water column since 2002 for time-period between April 2004 and October 2012. (b) Difference between the two time-series in (a). The effect of C_{anth} accumulating in the water column since 2002 on ocean C_{anth} transports at 26.5°N on ten-day (blue) and three month low-pass (black) time scales.

Method	Year	C_{anth} Transport ($Pg\ C\ yr^{-1}$) & Contribution to storage[a]	Storage ($Pg\ C\ yr^{-1}$)	Air-sea C_{anth} flux ($Pg\ C\ yr^{-1}$) & Contribution to storage	Citation
FROM GLOBAL ESTIMATES					
Biogeochemical Model	2000	0.15 ± 0.01	-	-	20
	2007	0.09 ± 0.02 (31%)	0.29	0.20 (69%)	19
Ocean Inversion	1995	0.12 ± 0.01 (33%)	0.39	0.28 (67%)	18
Ocean assimilation	2004	0.12 ± 0.01 (27%)	0.47	0.35 (73%)	10
Observational Integration	2000	-	0.38	-	4
FROM SYNOPTIC OBSERVATIONS					
Hydrographic sections	1992	0.24 ± 0.08 (58%)	0.43	0.18 (42%)	16
	1992	0.23 ± 0.08 (122%)	0.19-0.43[b]	-0.05 to 0.19 (-26 to 44%)	14
	1992	0.17 ± 0.06 (82%)	0.22[c]	0.04 (18%)	13
	1992	0.20 ± 0.02			17
	1998	0.20 ± 0.08 (95%)	0.22[c]	0.01 (5%)	13
	2004	0.25 ± 0.05 (66%)	0.39	0.13 (24%)	15
	2011	0.25 ± 0.02			17
This study	2004 to 2012	0.191 ± 0.013 47% to 41 %	0.39-0.47 [d] to 0.45-0.53 [d]	0.19-0.27 (~53%) to 0.25-0.33 (~59%)	
	2004	*0.16 ± 0.08 (36%)*[e]	*0.430* [d]		
	2005	*0.22 ± 0.07 (50%)*[e]	*0.438* [d]		
	2006	*0.22 ± 0.06 (49%)*[e]	*0.445* [d]		
	2007	*0.21 ± 0.06 (46%)*[e]	*0.453* [d]		
	2008	*0.20 ± 0.07 (43%)*[e]	*0.460* [d]		
	2009	*0.12 ± 0.09 (25%)*[e]	*0.468* [d]		
	2010	*0.19 ± 0.08 (40%)*[e]	*0.475* [d]		
	2011	*0.23 ± 0.06 (48%)*[e]	*0.483* [d]		
	2012	*0.20 ± 0.08 (41%)*[e]	*0.490* [d]		

Table 1. Summary of historical estimates of C_{anth} transport across 26.5°N, and storage / air-sea flux terms derived from North Atlantic C_{anth} budgets. [a]Relative contribution to storage reflects total oceanic C_{anth} transport and thus includes Bering Strait contribution. [b]Storage range calculated following ref [14], using range of surface layer carbon change of 0.75-1.75 μmol kg^{-1}. [c]Storage term calculated as residual of other components (transport, air-sea fluxes). [d]Storage estimates for 2004 (and scaled to 2012) from refs [10] and [18]. [e]Annual averages are calculated on an April to March basis due to time-series beginning in April 2004; contributions to storage are calculated as an average from different storage estimates.

Variable	Volume transport		Transport-weighted C_{anth}		C_{anth} transport		Contribution to C_{anth} transport trend due to:	
	Mean (std dev)	Trend (std err)	Mean (std dev)	Trend (std err)	Mean (std dev)	Trend (std err)	Volume transport changes	C_{anth} field changes
	Sv	Sv yr^{-1}	μmol kg^{-1}	μmol kg^{-1} yr^{-1}	Tg C yr^{-1}	Tg C yr^{-2}	Tg C yr^{-2}	Tg C yr^{-2}
Florida Straits	31.58 (2.71)	-0.091 (0.062)	54.4 (3.9)	1.57 (0.0001)	634 (68)	17 (1.3)	-2	19
Ekman	3.53 (2.56)	0.002 (0.059)	74 (9.2)	1.19 (0.2)	97 (71)	2 (2)	0.1	2
Interior:								
- 0-1100 db minus Ekman	-18.37 (3.43)	-0.476 (0.074)	65.6 (4.4)	0.86 (0.09)	-453 (76)	-18 (1.5)	-12	-6
- 1100-3000 db	-12.25 (2.26)	0.004 (0.052)	16.7 (1.52)	0.38 (0.03)	-77 (17)	-2 (0.4)	0	-2
- 3000-5000 db	-6.45 (2.82)	0.477 (0.059)	4.4 (1.18)	0.11 (0.03)	-10 (4)	0.6 (0.1)	0.8	-0.3
Total					191 (79)	-0.4 (2)	-11	11
Horizontal	0 (0)	0 (0)			-114 (20)	5 (0.4)	0	5
Overturning	17.21 (4.13)	-0.55 (0.09)			312 (88)	-6 (2)	-10	4

Section average C_{anth} concentration: 14.7 μmol kg^{-1} in 2004 to 17.1 μmol kg^{-1} in 2012

Table 2. Averages and trends for different components of anthropogenic carbon transports, volume transports, and transport-weighted anthropogenic carbon concentrations with associated standard deviation / standard error estimates, and their contribution to C_{anth} transport trends. Transport-weighted C_{anth} concentrations are calculated by dividing the C_{anth} transport by the volume transport. Volume transport values come from ref [23]. The interior relates to the ocean east of the Bahamas (essentially all transport excluding Florida Straits). 1000 Tg C = 1 Pg C.

METHODS

Hydrographic Data. Dissolved inorganic carbon (DIC), total alkalinity, oxygen, dissolved inorganic nutrients [nitrate, phosphate, silicate], CFC-12 and salinity from bottle samples combined with temperature and pressure data from CTD sensors were used from repeat cruises at 24.5°N in 1992[14,36], 1998[13], 2004[37], 2010[38] and 2011[39] and across Florida Straits in 2012[40]. Data consistency was ensured by comparing with historical data as part of GLODAPv2.2019[41]; all adjustments identified were applied. Anthropogenic carbon was calculated for each bottle using four techniques (φCT_o[42], TrOCA[43], ΔC^*[44], Transit Time Distributions-TTD[45]) following established methods[39]. Although its representativeness is questioned[46] TrOCA was included to enable comparison with previous studies[9,39,42].

Mixed layer bottle locations (density within $\sigma\theta = 0.03$ kg m^{-3} of the surface[47]) were treated separately as here traditional techniques struggle to quantify C_{anth} and its seasonal cycle - either relationships between nutrient utilisation, remineralisation and oxygen concentrations (used within back-calculation methods) break down, or the behaviour of CFCs and CO_2 (used by TTD and ΔC^* methods) decouple[48] due to their saturation state being dependent on distinct processes e.g. temperature (both), biology and R*f* (carbon only). Mixed layer C_{anth} was therefore calculated using a new method: SPIDEr (Scaled PreIndustrial DisEquilibrium).

SPIDEr method for mixed layer anthropogenic carbon. This circumvents/corrects a number of assumptions inherent in many C_{anth} methods (e.g. constant preindustrial seasonal atmospheric CO_2 concentration, CO_2 disequilibrium unchanged from preindustrial era, oxygen at 100% saturation). Extended Data Figure 4 summarises the calculation pathway applied to individual

4°latitude x 5° longitude boxes between 24-28°N and 78-12°W, and an additional Florida Straits box (25-27°N, 80.2-79.3°W). It involves:

1. Calculating regional seasonal cycles in sea surface pCO_2 disequilibrium from modern observations: following ref [49], historical observations of contemporary sea surface fCO_2 are from the Surface Ocean Carbon Dioxide Atlas (SOCAT) database[50] and temporally-coincident atmospheric XCO2 mole fraction observations are from ref. [51]; both were converted to pCO_2[52] using in situ temperature and NCEP local sea-level atmospheric pressure fields[53] to generate regionally-specific ΔpCO_2 time-series. Mean annual ΔpCO_2 cycles were calculated by Fourier analysis; their removal from the sea surface timeseries revealed no significant trend between 2002-2012; the mean ΔpCO_2 cycle (winter-spring undersaturation, summer-fall oversaturation) was therefore considered representative of the observational period.

2. Seasonal ΔpCO_2 cycles adjusted to preindustrial era by estimating the difference between the impact of physical (temperature/salinity) and biological (nutrient) changes on modern and preindustrial carbon concentrations. Spring-to-fall changes in temperature/salinity were calculated from climatological data[54] and applied to annual mean climatological chemical properties (DIC, alkalinity, salinity, nutrients[54]) using CO2SYS[55] to propagate their impact on ΔpCO_2. The impact of biological activity was estimated using winter-to-summer changes in phosphate converted to ΔDIC using a C:P stoichiometric ratio of 117 following the 'ΔC^*' C_{anth} method – this integrative C:P estimate has been successfully applied in the Atlantic and globally to derive C_{anth} fields and enhance intercomparison of studies[4,29,56], but likely underestimates true system variability[57]; ΔDIC was then applied to annual mean climatological chemical properties (temperature, alkalinity, salinity[54]) using CO2SYS[55] to calculate biologically-mediated ΔpCO_2. Both steps were repeated for a preindustrial scenario by removing the mean annual C_{anth} signal

(calculated using the φCT_o method applied to climatological data) from contemporary DIC levels; changes in preindustrial pCO_2 caused by temperature or biological activity were 69-72% of the change in pCO_2 observed at contemporary DIC levels.

3. Preindustrial ΔpCO_2 seasonal cycles are combined with estimated preindustrial atmospheric CO_2 seasonal cycles to generate 4°latitude x 5° longitude box-specific preindustrial seawater pCO_2 cycles. Preindustrial atmospheric CO_2 is calculated from modern GLOBALVIEW-CO2 atmospheric CO_2[51] combined with NCEP/NCAR temperature and sea level pressure fields[53] and deconvolved into a long-term atmospheric C_{anth} increase and a seasonally variable natural background signal.

4. Using in situ alkalinity and nutrients (assumed unaffected by anthropogenic CO_2 invasion) with preindustrial pCO_2 at the time of year of the modern measurements, the water sample's preindustrial DIC is calculated.

5. The residual between preindustrial and contemporary DIC concentrations is C_{anth}.

RAPID-MOCHA-WBTS-Argo array data. Ten-day temperature and salinity fields across 26.5°N[26] were used to calculate volume transports and 10-day C_{anth} fields. For the upper 1760 dbar, 0.25° longitude by 20 dbar grids of temperature and salinity are generated every 10 days by optimal interpolation of data from Argo floats and moored sensors; below 1760 dbar, salinity and temperature fields are linearly interpolated between moored sensors on the boundaries, with regions deeper than the moorings accounted for by extrapolation based on repeat hydrography abyssal structure. Volume transports were calculated by combining horizontal velocities from the gridded fields with circulation elements in the RAPID overturning calculation[21]. The UK-US RAPID array (Figure 1) uses submarine-cable-based transport estimates through Florida Straits at 27°N[58], ERA-Interim wind derived estimates of Ekman transport[59] and ocean interior transport estimates from moored data. The calculations generate a net volume (or freshwater) transport of 1.17 Sv southward across 26.5°N based on a salinity flux constraint at Bering Strait [26].

Predictive regression equations (PREs) for C_{anth}.

For each C_{anth} method, C_{anth} is determined for all available hydrographic bottle data prior to recalculating mixed layer values according to the SPIDEr approach. Linear C_{anth} growth rates were calculated in six isopycnal intervals (uNACW: σ_0<26.7 kg m^{-3}, lNACW: 26.7 kg m^{-3}<σ_0<27.2 kg m^{-3}, AAIW: 27.2 kg m-3<σ_0<27.6 kg m^{-3}, uNADW: σ_0>27.6 kg m^{-3} and σ_2<37 kg m^{-3}, lNADW: σ_2>37 kg m^{-3} and σ_4<45.9 kg m^{-3}, AABW: σ_4>45.9 kg m^{-3}) in five longitude ranges (Florida Straits, 78-70°W, 70-46°W, 46-30°W, 30-10°W)[39], and used to normalise all C_{anth} data to a mid-year of 2002.5. As the constituent data are from multiple seasons, the pooled normalised data cover a greater parameter range than individual hydrographic cruises, particularly in surface waters. Predictive regression equations (PREs) are generated by applying multiple linear regressions of the normalised C_{anth} according to normC_{anth} = a*θ + b*Sal + c*pres + d*lon + y^0, where a-d are predictive coefficients, ‘θ’ is potential temperature, ‘Sal’ is salinity, ‘pres’ is pressure, ‘lon’ is longitude and ‘y^0’ is a constant. Individual PREs are generated for each isopycnal-regional box as in Extended Data Fig. 1, with outliers identified using a 3x mean Cook’s Distance discriminating threshold and removed prior to rerunning. Extended Data Table 1 shows PRE coefficients for the ΔC* C_{anth} method. PRE root-mean-square errors (Extended Data Fig. 1b) are largest (but lowest relative to signal size) in surface layers where C_{anth} loadings and seasonal variability are highest, but are generally at or below C_{anth} estimation uncertainty (~6 μmol kg^{-1}). PRE goodness-of-fit (Extended Data Fig. 1c) shows greater variability, and highlights where either the predictive parameter is insufficiently covered by available measurements, or where the predictive parameters do not co-vary sufficiently with C_{anth}. PREs perform less well where C_{anth} levels change quickly with depth but temperature and salinity do not (typically ~800-1800 dbar, associated with C_{anth} minimum and maximum of Antarctic Intermediate Water and upper North Atlantic Deep Water respectively). PRE residuals are normal distributed about zero with no apparent vertical or spatial structure (Extended Data Fig. 2). However, PRE goodness-of-fit plots (Extended Data Fig. 3) display a general trend of regressions over(under)-estimating lower (higher) concentrations i.e. estimated values tend towards the isopycnic/regional box mean. The variability in available predictive parameter space (temperature, salinity, pressure, longitude) thus does not fully describe C_{anth} variability, but on a regional box basis uncertainties will likely cancel and errors in predicted values tend towards the regional C_{anth} mean. For all methods, analyses of standardised (Zscore) predictors identify salinity as the most important predictor variable, except in the upper layers away from the western boundary where temperature and pressure have similar influence.

10-day estimates of C_{anth}. For each 10-day period between spring 2004 and fall 2012, the predictive regressions are applied to temperature and salinity fields[26] derived from RAPID mooring / Argo float data (binned according to Extended Data Fig. 1a criteria) to estimate C_{anth}. The mixed layer is defined as the maximum mixed layer depth (MLD, determined using density within $\sigma\theta$ = 0.03 kg m^{-3} of the surface[47]) from the preceding winter – ensuring that winter waters temporarily isolated from atmospheric interaction during summer are still described by the same regression equation as the waters above, rather than falling within the bin below. Predicted surface layer C_{anth} (Extended Data Fig. 5 for 2009, 63.375°W) shows highest concentrations (late summer/early fall) associated with potential temperature maxima and neutral density, R*f* and MLD minima. The C_{anth} signal is diluted as cooling drives stratification breakdown, reaching a spring minimum as MLD (and R*f*) peaks. Pooled together, 10-day estimates of time-independent C_{anth} (normalized to 2002.5) are created. For each time-point ΔC_{anth} growth rates are reintroduced, using identical linear trends that normalized the original data set, generating final C_{anth} estimates reflective of the 2004-2012 time period.

C_{anth} transports across 26.5°N. 10-day C_{anth} and velocity fields are combined according to $T_{(Canth)}=\iint \upsilon C_{anth}\, dxdz$, where the C_{anth} transport, $T_{(Canth)}$, is given by the horizontal (x) and vertical (z) integral of the C_{anth} field multiplied by the velocity field υ[17]. The overturning transport component $T^{o}_{(Canth)}$ is calculated as $T^{o}_{(Canth)}=\int\langle\upsilon\rangle\langle C_{anth}\rangle dz$, where zonally-averaged fields of anthropogenic carbon $\langle C_{anth}\rangle$ and velocity $\langle\upsilon\rangle$ with section average removed are combined and vertically integrated (z) across the full section. The horizontal transport component $T^{h}_{(Canth)}$ meanwhile is calculated as $T^{h}_{(Canth)}=\iint \upsilon'\ C_{anth}'dxdz$, and is the horizontal (x) and vertical (z) integral of the combination of the deviation from the zonal-mean anthropogenic carbon C_{anth}' and velocity υ' fields. The throughflow component $T^{tf}_{(\mathrm{Canth})}$ is calculated as $T^{tf}_{(\mathrm{Canth})} = T^{tf}(C_{anth}'^{(26.5N)} - C_{anth}'^{(BS)})$ where C_{anth}' is the zonal-mean field for C_{anth} at 26.5°N (calculated here) and Bering Strait (BS, from ref [15]) and T^{tf} is the net volume throughflow transport. Florida Straits are treated separately; here, C_{anth} (including updated mixed layer C_{anth} estimates) from hydrographic sections in 2004, 2010 and 2012 (US GOMECC[40]) are combined with volume transport estimates derived from hydrographic CTD profiles. Transport-weighted C_{anth} estimates are used to create temporally-predictive regressions (Extended Data Fig. 6a) that are applied to the high frequency time-series of subsea cable-derived volume transport estimates. Combining Florida

Straits C_{anth} transports with ocean interior analogues yields 10-day C_{anth} transports across 26.5°N (Extended Data Fig. 6b,c). All C_{anth} methods show small, temporally-consistent systematic offsets from each other. These are due to slight differences in mean surface-to-depth C_{anth} gradients caused by the differing methodological assumptions of each technique. The TTD method is an exception; its offset changes with time, resulting from using CFC-12 alone to estimate mean water mass age. Decreasing atmospheric CFC-12 levels since ~2000 inhibit its ability to fully characterise the ventilation of the youngest waters, but it is the only transient tracer to have been measured on all hydrographic cruises with carbon data.

Uncertainties in C_{anth} transport estimates from observations. Following the approach used for salinity and freshwater transports across 26.5°N[26] the uncertainty of individual 10-day normalised C_{anth} transport estimates is calculated by estimating and combining C_{anth}-derived uncertainty (σCT_C) and transport-derived uncertainty (σCT_T). The uncertainty associated with both initial estimates of C_{anth} and the linear trends in C_{anth} (treated independently in the full section and Florida Straits) is then also assessed. The two combine to generate final C_{anth} transport uncertainties. For each subregion, σCT_C is calculated by combining the uncertainty in C_{anth} concentrations (σC_{reg}) with the average volume transport (T_{reg}). The transport-derived uncertainty is calculated by combining the subregional transport uncertainty σCT_T and the C_{anth} anomaly ($C_{reg} - C_{sect}$) where the C_{anth} section average is 19.2 µmol kg^{-1}. Uncertainties were calculated for individual regional water masses, the Bering Strait, Ekman layer, and Florida Straits[26] (Extended Data Table 2). Uncertainty relating to input C_{anth} fields and ΔC_{anth} trends was calculated by a Monte-Carlo approach: individual systematic offsets randomly-derived from a normal distribution of twice the estimation uncertainty (6 µmol kg^{-1}) were applied to each input hydrographic cruise dataset while similar offsets were applied to trends, randomly-derived from within the trend uncertainties[39]. The average standard deviation of 600 individual estimates at each timepoint gave an uncertainty of 0.037 Pg C yr^{-1}. Combining all the above uncertainties in quadrature generates an estimate of the total uncertainty for each 10-day C_{anth} transport estimate of 0.135 Pg C yr^{-1}. If it is assumed that within a year there can be 12 independent estimates of the C_{anth} transport, then uncertainty in the annual average C_{anth} transport is $0.135 / (12)^{1/2} = 0.039$ Pg C yr^{-1}. For the 8.5-year time-series there are then 102 independent estimates of the C_{anth} transport, meaning the uncertainty of the full time-series average C_{anth} transport is $0.135 / (102)^{1/2} = 0.0134$ Pg C yr^{-1}.

Uncertainties from surface C_{anth} seasonality calculation

The impact of not accounting for seasonality in surface C_{anth} concentrations was investigated by propagating 3 additional surface C_{anth} estimates to that described above through the C_{anth} transport calculation: 1. using unadjusted raw bottle C_{anth} estimates; 2. assuming C_{anth} to be 100% saturated at all times; 3. applying SPIDEr (Extended Data Figure 4), but assuming modern and preindustrial ΔpCO_2 cycles are identical. For 1. the C_{anth} seasonal cycle amplitude was ~3x larger than any other application (and implausible through what we know of sea-surface CO_2 flux dynamics); much higher C_{anth} concentrations for ~9-10 months of the year, resulted in elevated Ekman, horizontal and total C_{anth} transports (with full time-series average ~15% higher) and exaggerated seasonal cycles in each. A negligible horizontal transport trend led to the total C_{anth} transport trend becoming negative. For cases 2 and 3., a reversed seasonal cycle resulted: C_{anth} highest (lowest) in winter (summer), the opposite to that expected from R*f* variability[5,54]. In 2., a greatly reduced west-to-east gradient in C_{anth} concentrations resulted, leading to reduced southward horizontal circulation and a total transport average ~12% higher than that presented here. In 3., a west-to-east concentration gradient was maintained but at systematically higher concentrations; this generated stronger C_{anth} overturning and horizontal components but to differing extents, causing a net decrease in the average total C_{anth} transport of ~4% compared to results presented here. Failing to account for seasonality in CO_2 disequilibria and C_{anth} can therefore generate inverted seasonal cycles, and unfeasible concentration ranges and longitudinal gradients. These subsequently affect calculated Ekman, horizontal, overturning and total C_{anth} transports and their trends, and may be a factor in previous hydrographic section-derived C_{anth} transport estimates.

Uncertainties in C_{anth} transport estimates from PRE and C_{anth} methodologies. We test the robustness and appropriateness of the PRE method using an analysis of model data where model C_{anth} 'truth' is known. We use monthly fields from the 1° NEMOv3.2 ocean model with the MEDUSA-2 marine biogeochemistry model embedded[e.g.60], between 1980-2100 across 26.5°N. Model truth C_{anth} was calculated as the residual of parallel runs (with atmospheric growth of carbon and climate change effects at RCP8.5, and without), and combined with directly output velocity fields to give C_{anth} transports for 2004-2013 of 0.223 ± 0.061 Pg C yr^{-1} (mean ± standard deviation of monthly values). PRE-predicted C_{anth} fields (estimated using PRE methodology applied to model truth C_{anth}, temperature, pressure, salinity outputs as for observations) were combined with the same velocity fields, enabling direct comparison with model truth C_{anth} transports (Extended Data Fig. 7). Within this, several experiments were conducted, adjusting PRE data and trend inputs/treatments additively, to quantify the contributions of individual PRE methodological assumptions and their impact on the overall uncertainty in C_{anth} transport estimates. These were: (1) PRE method applied as for observations, using same vertical data resolution (~20 data points per station), input data timepoints (one month each from 1992-1998-2004-2010-2011), identical longitudinal/isopycnal boxes optimised to observational hydrographic distributions, and assuming linear ΔC_{anth} trends; (2) PRE regions optimised to model hydrographic distributions/transport fields (these differed significantly from observations due to low model resolution); (3) PRE training data extended to cover all months of years 1992-1998-2004-2010-2011; (4) non-linear ΔC_{anth} trends; and finally, (5) increased vertical data resolution (~60 data points per station). Iteration (1) resulted in a 2004-2013 C_{anth} transport mean ± standard deviation of 0.234 ± 0.059 Pg C yr^{-1}, a net residual from the model truth of 5% (0.011 Pg C yr^{-1}), with essentially identical monthly variability. Approximately 35% of the residual from model truth was explicable by insufficient vertical data resolution, ~23% by the assumption of linear C_{anth} growth rates, and the remainder due to PRE regions being poorly optimised to local hydrographic/transport fields. Iteration (2) was most faithful to the method's application to observations, and gave a 2004-2013 mean ± standard deviation of 0.229 ± 0.061 Pg C yr^{-1}, a 2.9% residual from model truth (0.223 ± 0.061 Pg C yr^{-1}). Individual monthly transport estimates had an average absolute residual of 4%, with best estimates in May-June (average 1.6% difference), poorest in September-October (average ~8.5% difference). Iteration (5) is considered the best estimate of the abilities of the PRE method – for 2004-2013 it reduced the mean to within 1% of model truth, and average absolute residuals of monthly estimates to 2.5%. This underlines the suitability of the PRE methodology in estimating the magnitude of C_{anth} transports over multiple timescales, and application to observational datasets.

'Back-calculation' C_{anth} estimation methods have been widely used to quantify the accumulation of C_{anth} in the oceans[e.g.4,5,9,13–15,17,37,39,42–44,56,61,62], and we applied three derivations based on biogeochemical parameters to observations. Of these we applied the ΔC^* method[44] to model outputs to test its effectiveness in estimating C_{anth} distributions and C_{anth} transport variability and magnitude compared to model truth. Ref [44] was followed for the calculation of 'ΔC^*', but using alternative parameterizations for preformed alkalinity[63] and preformed preindustrial DIC[62]. The disequilibrium term was determined from 'ΔC^*' derived from the model control run (with a preindustrial atmosphere). C_{anth} estimates were combined with model velocity fields and the resultant C_{anth} transports compared to model truth (Extended Data Fig. 8). A correlation of 0.97 between the two time-series occurred with an average residual of 2.2 $\times 10^{-4}$ Pg C yr^{-1} (0.5%) for the 2004-2013 period. Individual monthly transport estimates had mean absolute residuals of 7.2%, and annual average absolute differences of 0.010 Pg C yr^{-1} (4.5%). These differences are small, predominantly caused by control run 'ΔC^*' drift and deficiencies in the model's biogeochemical fields that impact the use of observation-based parameterizations, e.g. preformed alkalinity. Together, the estimates indicate that the back-calculation is useful for estimating C_{anth}.

DATA SOURCES

Raw hydrographic datasets are at https://cchdo.ucsd.edu/. Final adjusted hydrographic datasets are available from GLODAP (https://www.glodap.info/). AMOC estimates are available from the RAPID programme website (https://www.rapid.ac.uk/).

Atmospheric CO_2 is available from the GLOBALVIEW-CO2 web resources (GLOBALVIEW-CO2. Cooperative Atmospheric Data Integration Project - Carbon Dioxide; NOAA ESRL, Boulder, Colorado; Also available on Internet via anonymous FTP to ftp.cmdl.noaa.gov, Path: ccg/co2/GLOBALVIEW). Sea surface pCO_2 observations are from the Surface Ocean Carbon Dioxide Atlas SOCAT: https://www.socat.info/. NCEP/NCAR temperature and sea level pressure fields are available from https://psl.noaa.gov/data/gridded/data.ncep.reanalysis.surface.html.

DATA AVAILABILITY

The carbon transport data that support the findings of this study are available from the British Oceanographic Data Centre (https://www.bodc.ac.uk/) at https://www.bodc.ac.uk/data/published_data_library/catalogue/10.5285/b6bb9f45-f562-68a4-e053-6c86abc0e48b/. The doi of this dataset is 10.5285/b6bb9f45-f562-68a4-e053-6c86abc0e48b, and the data citation is : Brown P.J., McDonagh E., Sanders R., Watson A.J., Wanninkhof R.H., King B.A., Smeed D., Baringer M.O., Meinen C.S., Schuster U., Yool A., Messias M. (2020). Anthropogenic carbon transports at 26N as estimated using the RAPID-MOCHA-WBTS (RAPID-Meridional Overturning Circulation and Heatflux Array-Western Boundary Time Series) array for 2004 to 2012. British Oceanographic Data Centre - Natural

Environment Research Council, UK. doi: 10/fn4j. The dataset will also be accessible from the RAPID-Atlantic Biogeochemical Fluxes programme webpage (http://www.rapid.ac.uk/abc).

METHODS REFERENCES

35. Guallart, E. F., Pérez, F. F., Rosón, G. & Ríos, A. F. High spatial resolution Alkalinity and pH measurements along 24 . 5 ° N in 1992 Institut de Ciències del Mar , CSIC Passeig Marítim de la Barceloneta , 37-49 08003 Barcelona , Spain Instituto de Investigaciones Marinas , CSIC Eduardo Cabello , 6 Facultad . **5**, (2010).

36. Brown, P. J., Bakker, D. C. E., Schuster, U. & Watson, A. J. Anthropogenic carbon accumulation in the subtropical North Atlantic. *J. Geophys. Res.* **115**, C04016 (2010).

37. Schuster, U. *et al.* Measurements of total alkalinity and inorganic dissolved carbon in the Atlantic Ocean and adjacent Southern Ocean between 2008 and 2010. *Earth Syst. Sci. Data* **6**, 175–183 (2014).

38. Guallart, E. F. *et al.* Trends in anthropogenic CO2 in water masses of the Subtropical North Atlantic Ocean. *Prog. Oceanogr.* **131**, 21–32 (2015).

39. Wanninkhof, R. *et al.* Ocean acidification along the Gulf Coast and East Coast of the USA. *Cont. Shelf Res.* **98**, 54–71 (2015).

40. Olsen, A. *et al.* GLODAPv2.2019 – an update of GLODAPv2. *Earth Syst. Sci. Data* **11**, 1437–1461 (2019).

41. Vázquez-Rodríguez, M. *et al.* Anthropogenic carbon distributions in the Atlantic Ocean: data-based estimates from the Arctic to the Antarctic. *Biogeosciences* **6**, 439–451 (2009).

42. Touratier, F., Azouzi, L. & Goyet, C. CFC-11, Δ14 C and 3 H tracers as a means to assess anthropogenic CO 2 concentrations in the ocean. *Tellus B* **59**, 318–325 (2007).

43. Gruber, N., Sarmiento, J. L. & Stocker, T. F. An improved method for detecting

anthropogenic CO2 in the oceans. *Global Biogeochem. Cycles* **10**, 809–837 (1996).

44. Waugh, D. W., Hall, T. M., Mcneil, B. I., Key, R. & Matear, R. J. Anthropogenic CO 2 in the oceans estimated using transit time distributions. *Tellus B Chem. Phys. Meteorol.* **58**, 376–389 (2006).

45. Yool, A., Oschlies, A., Nurser, A. & Gruber, N. A model-based assessment of the TrOCA approach for estimating anthropogenic carbon in the ocean. *Biogeosciences* **7**, 723–751 (2010).

46. de Boyer Montégut, C., Madec, G., Fischer, A., Lazar, A. & Iudicone, D. Mixed layer depth over the global ocean: An examination of profile data and a profile-based climatology. *J. Geophys. Res.* **109**, C12003 (2004).

47. Álvarez, M. & Gourcuff, C. Uncoupled transport of chlorofluorocarbons and anthropogenic carbon in the subpolar North Atlantic. *Deep Sea Res. Part I Oceanogr. Res. Pap.* **57**, 860–868 (2010).

48. Landschützer, P. *et al.* A neural network-based estimate of the seasonal to inter-annual variability of the Atlantic Ocean carbon sink. *Biogeosciences* **10**, 7793–7815 (2013).

49. Bakker, D. C. E. *et al.* A multi-decade record of high-quality fCO2 data in version 3 of the Surface Ocean CO2 Atlas (SOCAT). *Earth Syst. Sci. Data* **8**, 383–413 (2016).

50. GLOBALVIEW-CO2. *Cooperative Atmospheric Data Integration Project - Carbon Dioxide; NOAA ESRL, Boulder, Colorado; [Also available on Internet via anonymous FTP to ftp.cmdl.noaa.gov, Path: ccg/co2/GLOBALVIEW]*. (2011).

51. Körtzinger, A. Methods of Seawater Analysis, Chap. Determination of Carbon Dioxide Partial Pressure (pCO2). *Verlag Chemie* 149–158 (1999).

52. Kalnay, E. *et al.* The NCEP/NCAR 40-Year Reanalysis Project. *Bull. Am. Meteorol. Soc.*

77, 437–471 (1996).

53. Takahashi, T. *et al.* Climatological distributions of pH, pCO2, total CO2, alkalinity, and CaCO3 saturation in the global surface ocean, and temporal changes at selected locations. *Mar. Chem.* **164**, 95–125 (2014).

54. van Heuven, S., Pierrot, D., Rae, J. W. B., Lewis, E. & Wallace, D. W. R. *MATLAB Program Developed for CO2 System Calculations, ORNL/CDIAC-105b*. (2011). doi:10.3334/CDIAC/otg.CO2SYS_MATLAB_v1.1

55. Gruber, N. Anthropogenic CO2 in the Atlantic Ocean. *Global Biogeochem. Cycles* **12**, 165–191 (1998).

56. Martiny, A. C. *et al.* Strong latitudinal patterns in the elemental ratios of marine plankton and organic matter. *Nat. Geosci.* **6**, 279–283 (2013).

57. Baringer, M. O. N. & Larsen, J. C. Sixteen years of Florida Current transport at 27 N. *Geophys. Res. Lett.* **28**, 3179–3182 (2001).

58. Dee, D. P. *et al.* The ERA-Interim reanalysis: configuration and performance of the data assimilation system. *Q. J. R. Meteorol. Soc.* **137**, 553–597 (2011).

59. Couldrey, M. P., Oliver, K. I. C., Yool, A., Halloran, P. R. & Achterberg, E. P. On which timescales do gas transfer velocities control North Atlantic CO2 flux variability? *Global Biogeochem. Cycles* **30**, 787–802 (2016).

60. Álvarez, M., Ríos, A. F., Pérez, F. F., Bryden, H. L. & Rosón, G. Transports and budgets of total inorganic carbon in the subpolar and temperate North Atlantic. *Global Biogeochem. Cycles* **17**, 1002 (2003).

61. Lee, K. *et al.* An updated anthropogenic CO2 inventory in the Atlantic Ocean. *Global Biogeochem. Cycles* **17**, art. no.-1116 (2003).

62. Brewer, P. G., Bradshaw, A. L., Shafer, D. K. & Williams, R. T. Measurements of total carbon dioxide and alkalinity in the North Atlantic Ocean in 1981. in *The Changing Carbon Cycle: A Global Analysis* (eds. Trabalka, J. R. & Reichle, D. E.) 348–370 (Springer, 1986).

EXTENDED DATA LEGENDS

Extended Data Figure 1. PRE regions and performance statistics. (a) Data bin locations for generation of independent predictive multiple linear regressions for C_{anth} estimation, (b) individual predictive PRE root mean square error, and (c), individual predictive PRE R^2 for each data bin for ΔC^* C_{anth}. Box colors and numbers relate to Extended Figures 3 & 4.

Extended Data Figure 2. PRE residuals (predicted C_{anth} – bottle C_{anth}) plotted against depth. a, for individual PREs, **b**, for all outputs binned, for ΔC^* C_{anth}. Numbers and colors relate to regions in Extended Data Figure 1a. Dots relate to Western basin, circles to Eastern basin

Extended Data Figure 3. Bottle C_{anth} estimates versus PRE predicted C_{anth} for ΔC^* C_{anth}. Numbers and colors relate to regions in Extended Data Figure 1a. Black lines indicate unity. Red lines indicate linear least squares fit of bottle estimates versus predicted. Dots relate to Western basin, circles to Eastern basin

Extended Data Figure 4. Schematic of PreIndustrial DisEquilibrium (SPIDEr) mixed layer C_{anth} calculation. Blue colour implies preindustrial era, yellow colour implies modern era. Numbers on left refer to explanations in Methods text.

Extended Data Figure 5. Variability in predicted surface layer C_{anth}. For 2009 at 62.375°W with C_{anth} plotted against **a**, pressure, **b**, neutral density and **c**, potential temperature. Color refers to time of year.

Extended Data Figure 6. C_{anth} transports across Florida Straits and 26.5°N. a, transport-weighted C_{anth} transports and volume transports for Florida Straits in 2004, 2010 and 2012. Lines are linear predictive fits. TTD has no data for 2012. **b**, C_{anth} transports across 26.5°N on 10-day (thin lines) and 3-month filtered (thick lines) timescales for 2004.3-2012.8 for four C_{anth} calculation methods with 2004-2012 averages and standard deviation.

Extended Data Figure 7. Application of C_{anth} transport calcaultion methodology to model outputs. Anthropogenic carbon transports (a,c) and their residual from the model truth (b,d) for 1980-2100 (a,b) and 2004-2013 (c,d) for five unique applications of the PRE methodology applied to 1° NEMO-MEDUSA model outputs. Legend lists colour schemes of model truth, and different modifications of PRE methodology applied. For conversion of carbon transports, 660 kmol s^{-1} = 0.25 Pg C yr^{-1}.

Extended Data Figure 8. Application of back-calculation C_{anth} methodology to model outputs. Top: Anthropogenic carbon transports for 1980-2100 for 1. application of ΔC^* C_{anth} calculation method to 1° NEMO-MEDUSA model outputs combined with model velocity fields, and 2. model truth. Bottom, as for top but for 2004-2013. Monthly values and 12-month running mean shown for both. For conversion of carbon transports, 660 kmol s^{-1} = 0.25 Pg C yr^{-1}.

Extended Data Table 1. Predictive coefficients a-d and constant y^0 from PREs for individual bins, according to normC_{anth} = a*θ + b*Sal + c*pres + d*lon + y^0, where ‘θ’ is potential temperature (°C), ‘Sal’ is salinity, ‘pres’ is pressure (dbar), and ‘lon’ is longitude (°E). Results here are from ΔC^* C_{anth} outputs.

Extended Data Table 2. C_{anth} transport uncertainty estimates. Key to column headings: σT_{reg}, uncertainty in regional transport; $C_{\_reg}$, regional C_{anth} average; $C_{\_sect}$, section C_{anth} average; ($C_{\_reg} - C_{\_sect}$), regional C_{anth} anomaly; σCT_T, C_{anth} transport transport-related uncertainty; $\sigma C_{\_reg}$, uncertainty in regional C_{anth} average; T_{reg}, regional transport; σCT_C, uncertainty in C_{anth} transport due to uncertainty in C_{anth}; σCT, total uncertainty. Section-averaged C_{anth} (C_{sect}) is estimated as 18.8×10^{-6} kmol m^{-3} (~18 µmol kg^{-1}). Combining in quadrature, each 10-day estimate of C_{anth} transport has an uncertainty of 0.135 Pg C yr^{-1}. Assuming that there are 12 independent estimates in the year then the uncertainty on the annual average C_{anth} transport is 0.135 Pg C yr$^{-1}/(12)^{1/2}$ = 0.039 Pg C yr^{-1}. Assuming there are 102 independent estimates across the full 8.5-year time-series then the uncertainty on the full time-series average C_{anth} transport is 0.135 Pg C yr$^{-1}/(102)^{1/2}$ = 0.013 Pg C yr^{-1}.

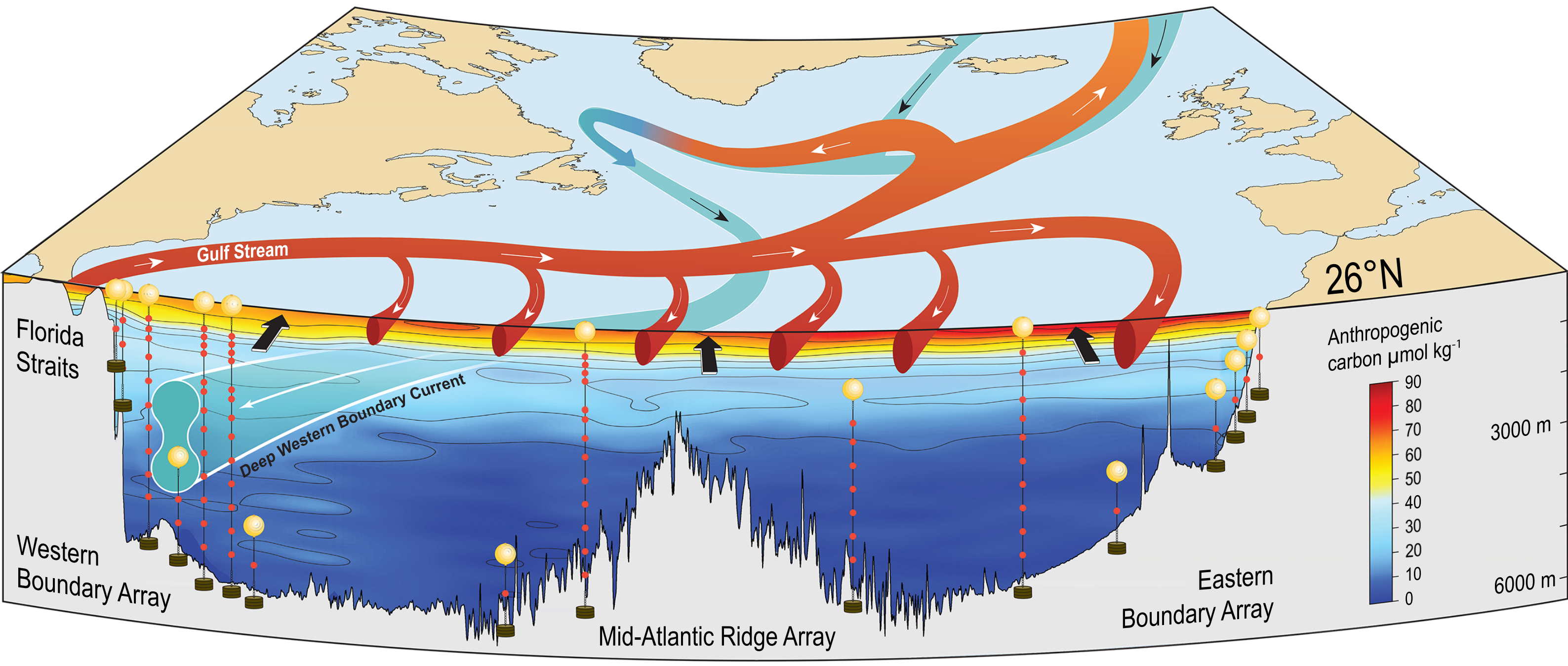

Gulf Stream
26°N
Florida
Straits
Deep Western Boundary Current
Anthropogenic
carbon µmol kg-1
90
80
70
60
50
40
30
20
10
0
3000 m
6000 m
Western
Boundary Array
Mid-Atlantic Ridge Array
Eastern
Boundary Array

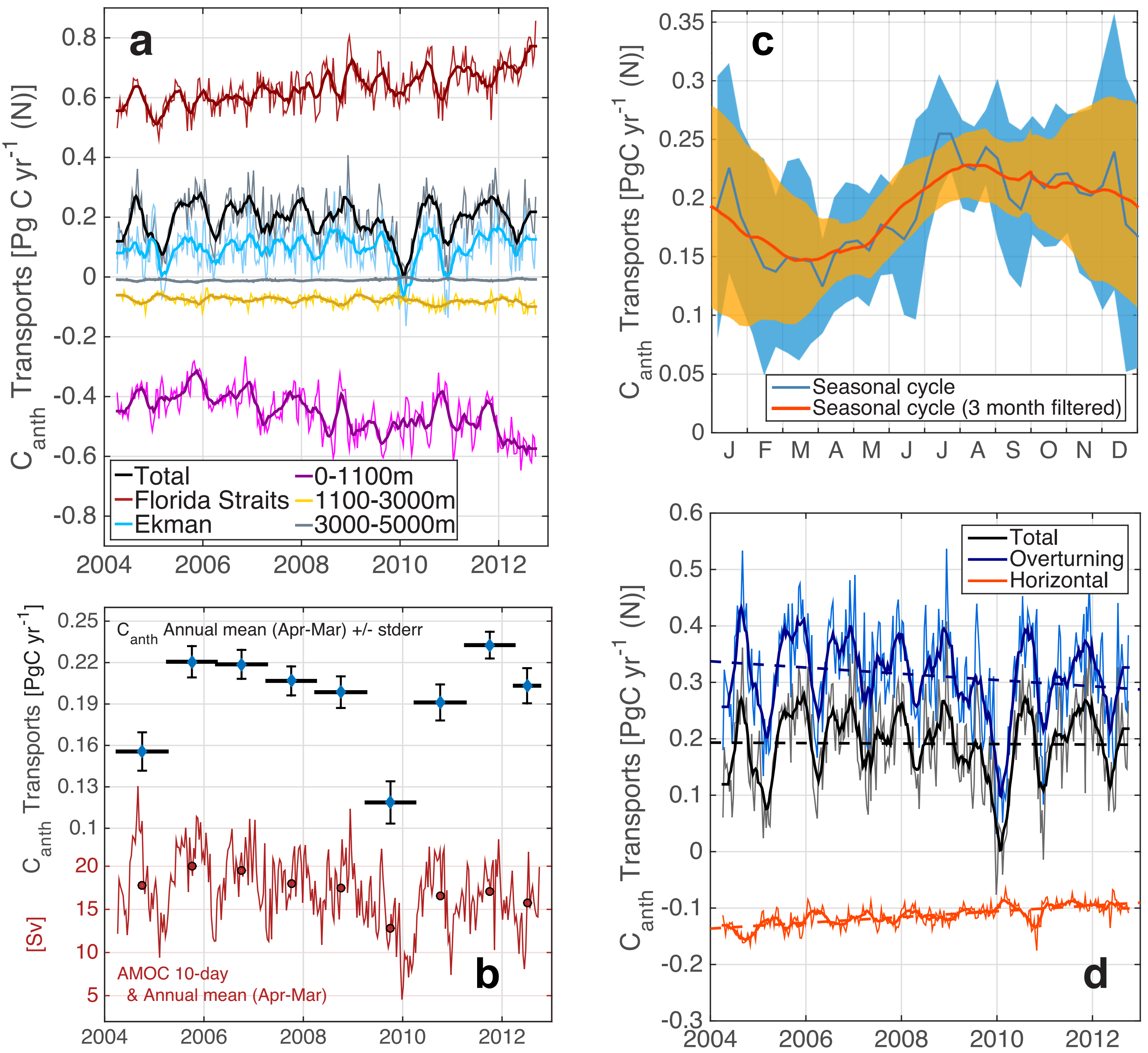

a
b
c
d
C_{anth} Transports [Pg C yr^{-1} (N)]
Total
Florida Straits
Ekman
0-1100m
1100-3000m
3000-5000m
C_{anth} Transports [PgC yr^{-1}]
C_{anth} Annual mean (Apr-Mar) +/- stderr
[Sv]
AMOC 10-day
& Annual mean (Apr-Mar)
C_{anth} Transports [PgC yr^{-1} (N)]
Seasonal cycle
Seasonal cycle (3 month filtered)
J F M A M J J A S O N D
Total
Overturning
Horizontal

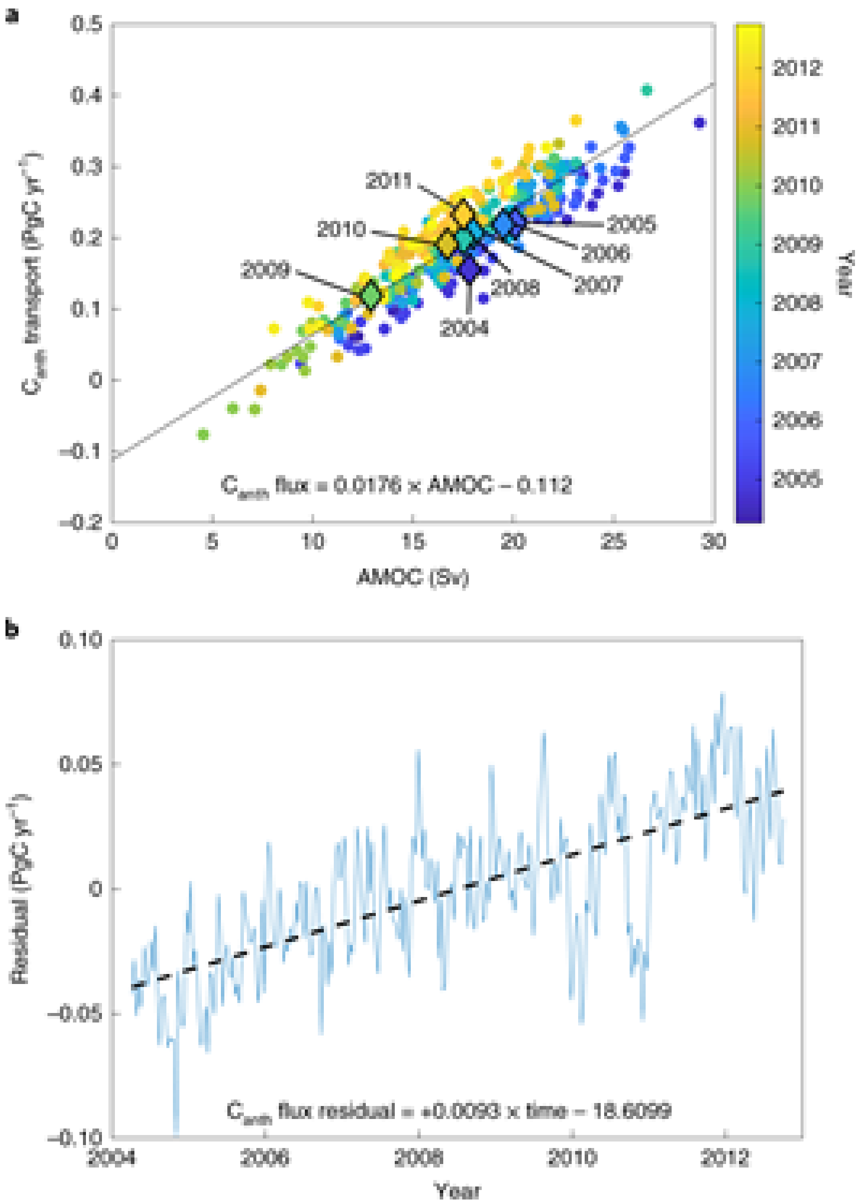
a
b
2011
2010
2009
2005
2006
2007
2008
2004
C_{anth} flux = 0.0176 × AMOC − 0.112
C_{anth} transport (PgC yr^{-1})
AMOC (Sv)
Year
Residual (PgC yr^{-1})
C_{anth} flux residual = +0.0093 × time − 18.6099

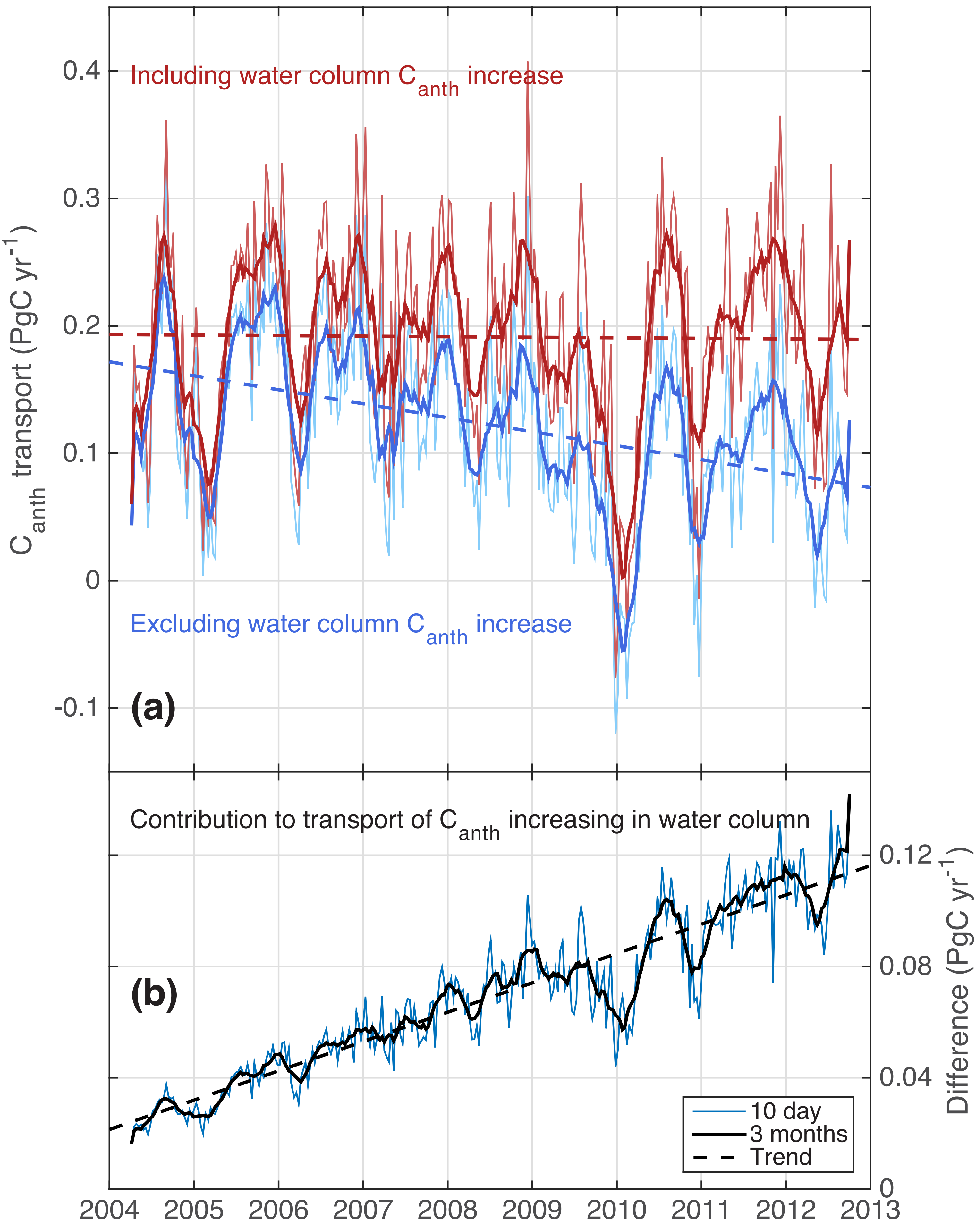

Including water column C_{anth} increase
Excluding water column C_{anth} increase
(a)
C_{anth} transport ($PgC\ yr^{-1}$)
0.4
0.3
0.2
0.1
0
-0.1
Contribution to transport of C_{anth} increasing in water column
(b)
Difference ($PgC\ yr^{-1}$)
0.12
0.08
0.04
0
10 day
3 months
Trend
2004
2005
2006
2007
2008
2009
2010
2011
2012
2013